TEXTURE-INDUCED CAVITATION BUBBLES AND FRICTION REDUCTION IN THE ELROD-ADAMS MODEL

Hugo M. Checo[a], Alfredo Jaramillo[a],
Mohammed Jai[b], Gustavo C. Buscaglia[a]

(a) Inst. de Ciências Matemáticas e de Computação, Univ. São Paulo, 13560-970 São Carlos, Brazil

(b) ICJ, INSA de Lyon (Pôle de Mathématiques), 69621 Villeurbanne, France

June 10, 2014

Abstract

We consider a thrust bearing consisting of an infinitely-wide pad, subject to a constant load and sliding at constant speed on a runner with transverse sinusoidal textures. The analysis method consists of time- and mesh-resolved simulations with a finite volume approximation of the Elrod-Adams model. Friction and clearance contours as functions of the texture depth and wavelength are built by performing more than ten thousand simulations. Conclusions are drawn for bearings of low, moderate and high conformity, unveiling basic mechanisms of friction reduction and global quantitative trends that are useful for texture selection.

Keywords: Textured bearings, Elrod-Adams model, Friction reduction, Cavitation, Numerical simulation.

Symbol	**Description**
a, b	the pad occupies the region $a < x < b$
d	texture depth
d_{lub}	lubricant film thickness at inlet boundary
f	instanteneous friction coefficient
$\overline{f}$	time-averaged friction coefficient
g	function controlling the onset of friction in the Couette term
h	clearance between runner and pad (in the z direction)
h_L	function describing the texture shape
h_U	function characterizing the pad profile

m	pad linear mass per unit width
p	hydrodynamic pressure
t	time variable
u	relative velocity between the pad and the runner
x, z	coordinate directions
x_ℓ,x_r	left and right boundaries of the computational domain
L	pad length
C	minimum clearance
F	friction force per unit width
H	non-dimensionalization length for z, Z and e
R	curvature radius of the pad's profile
U	non-dimensionalization for the relative velocity u
W^a	applied load per unit width
W^h	hydrodynamic force per unit width
Z	pad position in the z direction
θ	saturation variable
θ_s	threshold for the onset of friction in the Couette term
λ	period of textures
μ	dynamic viscosity
Σ	cavitation boundary
Ω^0	cavitated region
Ω^+	pressurized region

1 INTRODUCTION

Textured tribological surfaces have attracted much attention of the research community lately. After a significant number of experimental and theoretical studies, the possibility of reducing friction by means of microtextures has been established, together with a basic understanding of why this happens (at least in the hydrodynamic regime)[1–4].

That certain textures reduce friction in some hydrodynamic bearings is by no means an obvious phenomenon. Buscaglia et al[5,6] performed asymptotic analyses of general smooth (i.e., untextured) surfaces by introducing short-wavelength periodic perturbations of arbitrary shape and obtained that the untextured shape *always* maximizes the load carrying capacity and minimizes the friction coefficient. This implies that, for friction reduction to take place, there exist two possibilities: It can be a consequence of a *finite* perturbation (outside the validity of asymptotic theory), *or* involve physical mechanisms which

were not considered in the aforementioned mathematical studies, such as *cavitation*.

In a recent study, Checo et al[4] discussed several hundred numerical simulations and concluded that in fact *both* of the previous possibilities hold true in textured bearings that exhibit less friction than their untextured counterparts. As had already been advanced by Etsion[3], friction reduction only occurs in high-conformity bearings, in which the surfaces are so parallel that a texture of some suitable size and depth manages to produce local cavitation.

High-conformity bearings are not unfrequent in technology. Assuming a bearing of length L with a nominally planar surface opposing a surface with curvature radius R, the degree of conformity can be measured by the quotient R/L. For the compression ring of an internal combustion engine R/L is already quite high (about 40)[2], and it is much higher for other piston rings (oil rings in particular) and for other contacts such as seals.

It was numerically shown by Gadeschi et al[2] with a non-mass-conserving model, and later by Checo et al[4] with a mass-conserving model, that for a given load the minimal friction is in general obtained with a moderate R/L ratio (of the order of 10). Further, their results indicate that moderate-conformity contacts cannot be improved by texturing the surfaces.

Their numerical findings also show, on the other hand, that high-conformity contacts can indeed be improved by texturing. The friction cannot be reduced to the point of becoming smaller than that of smooth bearings with moderate conformity, but nevertheless significant reduction appears to be achievable. These findings are consistent with pioneering experimental results of Costa & Hutchins[7], and with more recent studies by Kovalchenko et al[8], Yin et al[9], Tomanik[10], Scaraggi et al[11], among others[12–15].

Friction-reducing texturing is especially practical when the texture is placed on the surface that exhibits less wear (e.g.; the runner of a thrust bearing, the cylinder liner of a ring/liner contact[10]). The reason for this is that, since the curvature radius R increases with wear, the texture (if undamaged) becomes more beneficial as time evolves.

However, though the general picture seems to be coming to a consensus, little is still known about the actual physical mechanisms that take place at a cavitating microtextured contact. Detailed quantitative assessments that allow for the practical selection of a suitable texture for a specific device are also very scarce.

For these reasons, in this article we go back to the basics and study the arguably simplest bearing: an infinitely-wide thrust bearing with a circular-arc-shaped pad. This bearing is assumed sliding on a runner with the arguably simplest texture: a sinusoidal one. The study is conducted with Elrod-Adams model, which though not free of criticism[16,17], is the most accepted model for hydrodynamic lubrication with cavitation. This model is mass-conserving, a property that as shown by Ausas et al[18] is crucial for obtaining realistic results when simulating textured bearings. The finite volume code that implements the model is thoroughly described by Ausas et al[19].

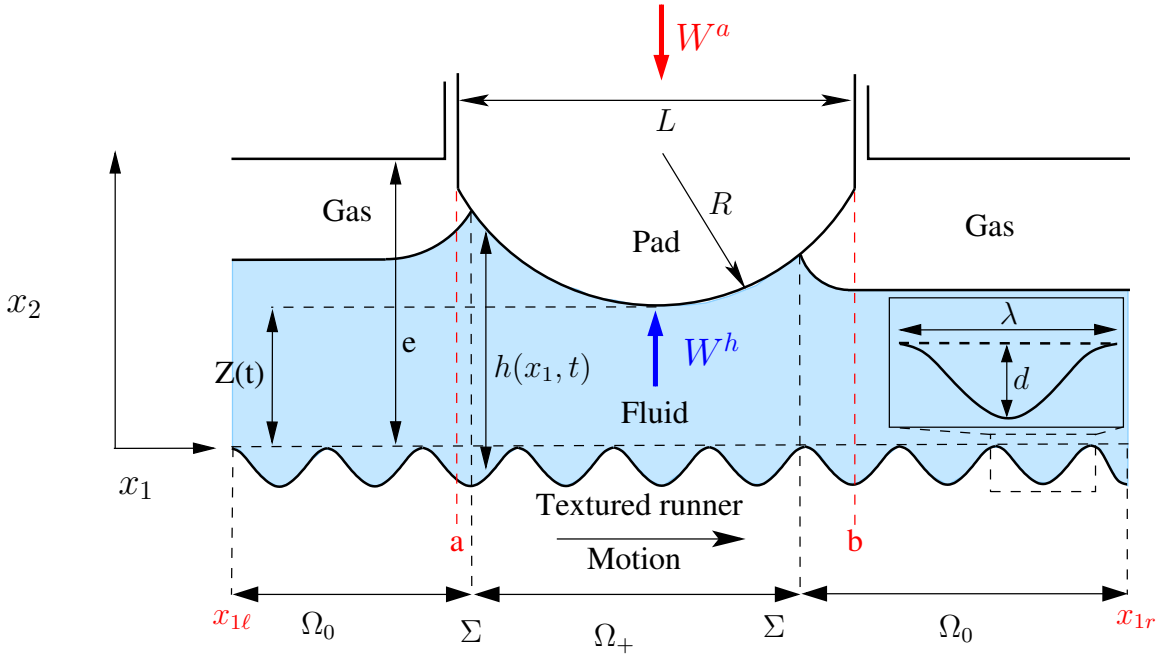

Figure 1: Scheme of a the domain along the pad's direction of motion, with the forces acting on it.

The plan of this paper is as follows: In Section 2 we briefly recall the Elrod-Adams model and introduce the problem under consideration and its non-dimensionalization. Section 3 discusses the numerical aspects of the work and the general setting of the computational experiments. Section 4 is devoted to reporting and discussing the numerical results, by first providing detailed analyses of three representative cases and then showing extensive charts of friction coefficient and clearance as functions of the problem parameters. The basic mechanism of friction reduction identified in this work is a local pressurization of the convergent microwedges at each texture cell, accompanied by local cavitation at the divergent microwedges. The cavitation bubble that forms at each texture cell is crucial for preventing the appearance of local negative pressure peaks that would cancel out the positive lift force generated at the convergent microwedges. This is consistent with mechanisms suggested by other authors[2,20], and puts forward the importance of cavitation bubbles. Section 5 is devoted to a thorough discussion of the numerical results, identifying and interpreting trends in the predictions of the model. Concluding remarks are left for Section 6.

2 MODEL

As shown in Fig. 1, the direction of the motion of the pad is chosen to be x, parallel to the runner surface. The textures on the runner are given by a function $z = -h_L(x) \leq 0$ ($h_L(x)$=0 for the untextured liner).

A single pad with a profile $h_U(x)$ is assumed sliding with constant velocity $-u$ against the runner.

The pad is free to move vertically under the applied forces. The profile $h_U(x)$ satisfies

$$\min h_U(x) = 0$$

and its analytical expression corresponds to an arc of circumference of radius R. The computational domain is attached to the pad, which is assumed to be of length L and to extend between $x = a$ and $x = b$. The runner thus moves in the positive x direction with constant velocity u. Outside of the pad's location the gap between the surfaces is assumed uniform of thickness e, large enough not to affect the results. The (artificial) simulation boundaries are located at $x = x_\ell < a$ and $x = x_r > b$.

Under the assumptions above, the gap between the pad and the runner is given by

$$h(x,t) = \begin{cases} h_L(x - u\,t) + h_U(x) + Z(t) & \text{if } \; a < x < b \\ h_L(x - u\,t) + e & \text{otherwise} \end{cases} \tag{1}$$

where $Z(t)$ denotes the vertical distance between the pad and the z=0 line. The instantaneous *clearance* $C(t)$ is defined as

$$C(t) \;=\; \min_{x\,\in\,(a,b)} \; h(x,t)$$

2.1 Hydrodynamics and cavitation modeling

We adopt the well-known Elrod-Adams model[21], which incorporates into a single formulation Reynolds equation for the pressurized region and Jacobsson-Floberg-Olsson boundary conditions. This model is mass conserving, which is essential for obtaining physically meaningful results in lubrication problems involving textured surfaces[18].

The model postulates the computation of two fields, p and θ, which correspond to the hydrodynamic pressure and to an auxiliary saturation-like variable, respectively, that (weakly) satisfy the equation

$$\frac{\partial}{\partial x}\left(\frac{h^3}{12\mu}\frac{\partial p}{\partial x}\right) = \frac{u}{2}\frac{\partial\, h\theta}{\partial x} + \frac{\partial\, h\theta}{\partial t} \tag{2}$$

under the complementarity conditions

$$\begin{cases} p \;>\; 0 & \Rightarrow \quad \theta \;=\; 1 \\ \theta \;<\; 1 & \Rightarrow \quad p \;=\; 0 \\ 0 \;\leq\; \theta \;\leq\; 1 & \end{cases} \tag{3}$$

where μ is the viscosity of the lubricant.

For the contact we assume that the lubricant-film thickness is known (and constant, equal to d_{lub}) far upstream of the pad. This amounts to imposing that $\theta = d_{\text{lub}}/h$ at the boundary of the computational

domain. More precisely, if the computational domain corresponds to $x_\ell < x < x_r$, then assuming $u > 0$ we impose $\theta(x_\ell, t) = d_{\text{lub}}/h(x_\ell, t)$. An initial condition for θ is also provided.

At each instant the domain spontaneously divides into a *pressurized* region, Ω^+, where $p > 0$, and a *cavitated* region, Ω^0, where the film is not full ($\theta < 1$, see Fig. 1). At the boundary between Ω^+ and Ω^0, the so-called cavitation boundary Σ, the Elrod-Adams model automatically imposes mass-conservation.

2.2 Pad dynamics and friction forces

The dynamics of the pad is governed by the forces acting on it along the z-direction. These forces are described below.

The *applied load* points downwards (i.e.; along $-z$) and is assumed constant. We denote by W^a its value *per unit width*.

The *hydrodynamic force* originates from the pressure $p(x,t)$ that develops in bearing. Its value per unit width is given by

$$W^h(t) = \int_a^b p(x,t)\ dx \tag{4}$$

All lubricant films obtained in the simulations are thick enough to exclude the possibility of direct contact between the pad and the runner. Solid-solid forces are therefore neglected.

If m is the mass of the pad per unit width, the dynamical equation for the pad's vertical displacement reads

$$m\frac{d^2Z}{dt^2} = -W^a(t) + W^h(t) \tag{5}$$

This is supplemented with initial conditions for Z and Z' at $t = 0$.

The friction force per unit width is given by

$$F = \int_a^b \left(\frac{\mu u\, g(\theta)}{h} + \frac{1}{2}h\frac{\partial p}{\partial x} + p\frac{\partial h_L}{\partial x} \right)\ dx \tag{6}$$

where the function $g(\theta)$ is taken as

$$g(\theta) \ = \ \theta\, s(\theta) \tag{7}$$

with $s(\theta)$ the switch function

$$s(\theta) = \begin{cases} 1 & \text{if } \ \theta > \theta_s \\ 0 & \text{otherwise} \end{cases} \tag{8}$$

In this friction model θ_s is a threshold for the onset of friction, interpreted as the minimum lubricant fraction needed for shear forces to be transmitted from one surface to the other. In all calculations the value $\theta_s = 0.95$ has been adopted. Choosing another value for θ_s has been shown to not alter the behavior of the contact significantly[4]. Notice from the definition of $g(\theta)$ that for $\theta > \theta_s$ the friction is

calculated with an "effective viscosity" equal to $\theta\,\mu$. The friction coefficient then results from

$$f = \frac{F}{W^a} \tag{9}$$

Remark: The term $p\frac{\partial h_L}{\partial x}$ is not a shear force. Instead, it corresponds to the projection of the pressure force along x when the normal to the liner is not along z. This term is omitted in the literature, which mostly considers textures on the pad. Notice that this term is necessary for the forces on the pad and on the runner to be equal and opposite (action-reaction principle).

2.3 Non-dimensionalization and final equations

We consider a non-dimensionalization of the equations based on a velocity scale U (taken as equal to u), a length scale L (taken as equal to the pad's length), and a film thickness scale H. No obvious candidate for H is available because we will be comparing results with different pad's curvatures and different texture depths, so that for now we leave H unspecified. All computations are non-dimensional.

The scales above, together with the viscosity μ of the lubricant, lead to the following derived scales for the different quantities

Table 1: Basic and derived scales

Quantity	Scale	Name
x,λ	L	horizontal coordinate, texture period
u	U	relative velocity
R	L	pad's profile curvature radius
t	$\frac{L}{U}$	time
h, C	H	gap thickness, minimum clearance
Z,d	H	pad's vertical position, texture depth
p	$\frac{6\mu UL}{H^2}$	pressure
W^a, W^h	$\frac{6\mu UL^2}{H^2}$	applied and hydrodynamic forces per unit width
F	$\frac{\mu UL}{H}$	friction force per unit width
m	$\frac{6L^4\mu}{H^3U}$	mass per unit width

Notice that, since the scales for radial and friction forces are different, the friction coefficient is given by

$$f = \frac{H}{6L}\,\frac{\hat{F}}{\hat{W}^a} \tag{10}$$

where the carets (hats) denote the corresponding non-dimensional quantity.

Upon non-dimensionalization of all variables, and omitting all carets for simplicity, the complete non-dimensional mathematical problem to be solved reads:

"Find trajectory $Z(t)$, and fields $p(t)$, $\theta(t)$, defined on $\Omega = (x_\ell, x_r)$, satisfying

$$\left\{ \begin{array}{l} Z(0) \;=\; Z_0, \qquad Z'(0) \;=\; V_0, \\ \theta(x_\ell, t) = d_{\rm lub}/h(x_\ell, t) \\ p \;>\; 0 \qquad \Rightarrow \qquad \theta \;=\; 1 \\ \theta \;<\; 1 \qquad \Rightarrow \qquad p \;=\; 0 \\ 0 \;\leq\; \theta \;\leq\; 1 \end{array} \right. \tag{11}$$

and

$$m \frac{d^2 Z}{dt^2} \;=\; -W^a + W^h(t) \tag{12}$$

$$\frac{\partial}{\partial x}\left(h^3 \frac{\partial p}{\partial x} \right) \;=\; u\, \frac{\partial\, h\theta}{\partial x} + 2\, \frac{\partial\, h\theta}{\partial t} \tag{13}$$

where

$$h(x,t) \;=\; \left\{ \begin{array}{ll} h_L(x - u\,t) + h_U(x) + Z(t) & \text{if } \; a < x < b \\ h_L(x - u\,t) + e & \text{otherwise} \end{array} \right. , \tag{14}$$

$$W^h(t) \;=\; \int_a^b p(x,t)\; dx \;, \tag{15}$$

and the functions $h_L(x)$ and $h_U(x)$ are known explicitly."

The formula for the non-dimensional friction force per unit width is:

$$F = \int_a^b \left(\frac{\mu u\, g(\theta)}{h} + 3h \frac{\partial p}{\partial x} + 6p \frac{\partial h_L}{\partial x} \right)\; dx \tag{16}$$

Notice the term $6\,p\,\frac{\partial h_L}{\partial x}$, which appears only when the texture moves across the domain and is omitted in much of the literature.

3 NUMERICAL METHOD AND DESCRIPTION OF NUMERICAL TESTS

The numerical treatment is exactly that described in Ausas et al[19]. It consists of a finite volume, mass-conserving method with upwinding discretization of the Couette flux and centered discretization of the Poiseuille flux, together with an iterative imposition of the cavitation conditions ($p \geq 0$; $\theta < 1 \;\Rightarrow\; p = 0$; $p > 0 \;\Rightarrow\; \theta = 1$) by means of a Gauss-Seidel-type algorithm. The dynamical equation (12) for $Z(t)$ is discretized by a Newmark scheme, which is built into the overall iterative process.

Although the study focuses on one-dimensional problems, it is only recently that numerical assess-

ments as detailed as those reported in this article have become affordable. Further, since we consider the texture to be on the runner and thus moving through the computational domain, the hydrodynamic simulation must be run in unsteady mode, with a small enough time step to capture the vertical oscillations of the pad as textures pass under it.

An effort has been made in this work to refine the space and time discretizations until the results become discretization-independent. Very fine spatial meshes are needed for this, because each texture cell needs to be discretized into one hundred or more finite volumes. The coarsest spatial mesh used consisted of 512 cells along x, and some simulations were double-checked with up to 4096 cells. Although the method is fully-implicit, a unit-CFL condition was enforced, leading to time steps that ranged from $\Delta t = 4 \times 10^{-3}$ to $\Delta t = 5 \times 10^{-4}$.

The many thousands of computer runs compiled in the next sections were made feasible by the high robustness of the algorithm implemented in our in-house code[19]), together with multigrid acceleration by the Full Approximation Scheme[22,23]and an effective shared-memory strategy. The typical running time of one simulation on the 512-cells mesh is about five minutes in a state-of-the-art desktop, while about three hours are needed for the finest mesh.

The numerical experiments consider velocity and applied load as constant. The runner's texture is assumed periodic, with period λ, i.e.;

$$h_L(x) = h_L(x + \lambda) \qquad \forall\, x$$

An initial transient takes place as the pad adjusts its average vertical position. This transient lasts between 1 and 8 time units. After it, the pad reaches a periodic vertical motion, with time period λ (notice that the non-dimensional velocity is $u \equiv 1$), and all quantities become periodic.

The contacting surface of the pad is assumed to be a sector of a circular cylinder of radius R, with R varying between 4 and 1024. Since the length of the pad is 1, radii R greater than about 128 correspond to essentially conformal contacts. A value $R \simeq 40$ is typical of compression rings in the automobile industry[2].

Let us analyze on what non-dimensional parameters the solution of the problem depends. Since we focus on the periodic regime, the initial conditions for θ, Z and Z' are irrelevant. In this first study we have decided not to address starvation effects. For this purpose, d_{lub} was chosen large enough to assure fully-flooded conditions, thus making this parameter also irrelevant. There only remain two parameters in the model: The mass per unit width m and the applied load W^a.

The default values that we select for these parameters are

$$m_0 = 2 \times 10^{-5} \qquad \text{and} \qquad W_0^a = 1.666 \times 10^{-4}$$

Along the experiments, other values were tested so as to assess the problem's sensitivity to the data.

When considering realistic scale values such as $U = 10$ m/s, $L = 10^{-3}$ m, $H = 1$ micron, $\mu = 4 \times 10^{-3}$ Pa-s, the value selected for m_0 corresponds to 0.048 kg/m, which is typical of compression rings in car engines.

The value selected for W_0^a, with the same scales as above, corresponds to an applied load of 40 N/m, also in the range of pre-stress loads of piston rings. A more popular non-dimensionalization of the applied load is provided by the Stribeck number S, defined by $S = \frac{\mu\, u}{W^a}$ (the quantities on the right-hand side are dimensional this time). Back to non-dimensional variables, the previous relation in our non-dimensionalization becomes

$$S = \frac{H^2}{6\, L^2}\ \frac{\hat{u}}{\hat{W}^a} \tag{17}$$

so that W_0^a corresponds to a Stribeck number $S_0 = 10^{-3}$.

Finally, let us define the main tribological quantities that will be extracted from the numerical simulations. The instantaneous friction coefficient $f(t)$ and clearance $C(t)$ depend periodically on time once the bearing has reached its periodic regime. The tribological quantities that will be considered representative of the periodic regime are the *average friction coefficient*

$$\overline{f}\ =\ \frac{1}{\lambda}\ \int_T^{T+\lambda} f(t)\ dt \tag{18}$$

which characterizes the power lost to friction, and the *minimum clearance*

$$C_{\min}\ =\ \min_{T \le t \le T+\lambda}\ C(t) \tag{19}$$

which can be used to characterize wear. In the previous definitions T is large enough for the bearing to have reached its periodic regime (i.e.; $T > 8$).

4 EFFECTS OF THE RUNNER'S TEXTURE

A large set of experiments was conducted in the simplified setting of one-dimensional transverse textures. Further, the runner was assumed to be sinusoidal of depth d, namely

$$h_L(x) = d\ \frac{1\ -\ \cos(2\,\pi\, x/\lambda)}{2} \tag{20}$$

(notice that h_L is a "depth" (positive downwards), so that it is minimal at crests and maximal at troughs). Such a runner was selected so as to observe the dynamics of the system under maximal smoothness of the contacting surfaces. The applied load was fixed at W_0^a corresponding to a Stribeck number $S = 10^{-3}$. At this load, the equilibrium clearance of the pad for an untextured runner depends on R as shown in Table

R	f	$C_{\min}$
4	7.607×10^{-2}	6.369
8	7.449×10^{-2}	7.809
16	8.122×10^{-2}	8.021
32	9.562×10^{-2}	7.408
64	1.189×10^{-1}	6.363
128	1.536×10^{-1}	5.231
256	2.030×10^{-1}	4.325
512	2.612×10^{-1}	3.695
1024	2.871×10^{-1}	3.324

Table 2: Friction coefficient f and clearance $C_{\min}$ for pad's with several values of R once they reached the equilibrium position over an *untextured* runner. The computations were made for a load $W^a = W_0^a$.

Case #	W^a	R	λ	d	$\overline{f}$	$C_{\min}$	V_f	V_C
1	1.66×10^{-4}	32	1	5	0.082	6.89	-14%	-7%
2	1.66×10^{-4}	32	0.1	5	0.114	5.66	+19%	-24%
3	1.66×10^{-4}	256	0.1	5	0.193	2.52	-5%	-42%
4	1.66×10^{-4}	256	1	5	0.084	6.33	-59%	+46%

Table 3: Details of the cases discussed in Sections 4. W^a stands for the applied load, m for the linear mass, R for the curvature radius of the pad, λ for the texture's period (wavelength), d for its depth, $\overline{f}$ for the numerically obtained average friction coefficient and $C_{\min}$ for the numerically obtained minimum clearance. V_f and V_C stand for the relative variations of $\overline{f}$ and $C_{\min}$ with respect to the untextured case. All quantities are non-dimensional. Notice that Case 4 is introduced in subsection 4.2.2.

2, which also shows the friction coefficient for each R. The minimal friction is obtained for $R = 8$, while the maximum clearance takes place for $R = 16$. Notice that for an untextured runner the equilibrium values of f and C do not depend on m.

4.1 General description of the intervening phenomena

The study was conducted for different values of the texture parameters d and λ, also considering different values of the pad's curvature radius R. The mass of the pad was fixed at $m = m_0$. Some selected cases are discussed below (see Table 3 for details of each case). Notice that some cases have rather large values of λ, of the order of the pad's length. Though this could be viewed as a "waviness" of the runner instead of as a texture, we keep the word "texture" for all values of λ.

Case 1: Consider first a ring with a moderate value of $R = 32$, sliding on a runner with a texture of period equal to the pad length ($\lambda = 1$) and depth $d = 5$. The system behavior is then periodic in time

with period equal to one. Redefining $t = 0$ as the instant at which the texture crest is exactly under the left edge of the pad, profiles of p and θ are shown in Fig. 2 for $t = 0$, 0.25, 0.5 and 0.75.

At $t = 0$ the crests of the texture coincide with the left ($x = 0.5$) and right ($x = 1.5$) edges of the pad, while the trough coincides with the pad's centerline ($x = 1$). Notice that, *since the texture is moving with the runner*, its *convergent* wedge corresponds to the sector between a crest and its neighboring trough *to its right*, where the upward normal is tilted *to the right*. This is the opposite to what occurs on the pad's surface, in which the *convergent* wedge corresponds to the left half of the pad, at which the (downward) normal is tilted to the left. Analogously, if the upward normal to the runner is tilted to the left this corresponds to a *divergent* wedge.

At $t = 0$, thus, the convergent wedge of the texture is located under the left half of the pad, coincident with the convergent wedge of the pad's surface. This leads to a pressure profile similar to that of the untextured case, but much larger in value. At $t = 0.25$ the pressure peak has moved to the right, accompanying the texture's convergent wedge, and the net effect is still that of increasing the average pressure under the pad. At $t = 0.5$ the texture's crest is under the pad's center, leaving the left half of the pad over the texture's divergent wedge and consequently at zero pressure. A cavitation bubble develops there, which is evident from the θ profile ($\theta < 1$ implies cavitation). This cavitation bubble, which first appears at $t \simeq 0.304$ and $x \simeq 0.514$, grows and moves to the right with the divergent wedge that generates it, passing under the pad's center and eventually leaving the pad to the right. In fact, this same cavitated region but corresponding to the previous texture cell can be observed leaving the pad at $t = 0.5$ (just notice the region with $\theta < 1$ near $x = 1.5$). The cavitated region is always located at the *divergent* wedge of the texture and travels with it. Its right boundary is a *rupture* boundary, and as expected θ is continuous there and $\partial p/\partial x = 0$. The left boundary of the cavitated region is a *reformation* boundary, and as such the θ profile is very steep there, and $\partial p/\partial x$ exhibits a jump.

Remark: It is worth pointing out that the profiles at $t = 0$ show a cavitation boundary at $x \simeq 1.15$ for both the textured and the untextured cases. This boundary is a *rupture* boundary in the untextured runner and a *reformation* boundary in the textured one.

Case 2: With the same pad ($R = 32$) and the same texture depth ($d = 5$), it is interesting to consider a texture size much smaller than the pad's length. Figure 3 shows profiles of p and θ at four instants of the periodic regime obtained with $\lambda = 0.1$. Since the time period is equal to λ, and again defining $t = 0$ when a crest is at the left edge of the pad, the instants shown in Fig. 3 correspond to $t = 0$, 0.025, 0.05 and 0.075.

In this case the convergent wedge of the pad dominates the pressure field in the left part of the contact. No cavitation bubbles form there, and the effect of the texture is merely a modulation of the pressure field with local maxima/minima at the convergent/divergent wedges of the runner, respectively. The right part of the contact, on the other hand, exhibits moving pressurized regions (local pressure peaks)

that are absent in the untextured case. The texture's convergent wedges generate locally pressurized regions, with cavitation bubbles between them, and all this structure moves to the right with the runner.

Remark: In fact, a careful analysis of the θ field near the left edge of the pad shows that a tiny cavitation bubble appears there when the divergent wedge of the texture enters the contact, but it collapses soon afterwards and has no significant effect on the pressure field. Cavitation bubbles that appear near the left edge and collapse (or not) under the pad are discussed further later on.

Case 3: The last case we consider in this general description corresponds to the same texture as before ($\lambda = 0.1$, $d = 5$), but now with a high-conformity pad ($R = 256$). The corresponding profiles of p and θ at times $t = 0$, 0.025, 0.05 and 0.075 are shown in Fig. 4. One observes that a cavitation bubble develops whenever the divergent wedge of a texture enters the contact, and that this bubble then travels with the texture until leaving the pad at its right edge. Also, a locally pressurized region develops at the convergent wedges of each texture and travels with it. The height of the pressure peaks are slightly modulated by the pad's shape, but there is no doubt that the overall solution is governed by the runner's texture. The cavitation bubbles generated at each texture impose a zero-pressure boundary condition for the pressurized region that develop at the convergent texture wedges. The global pressure field simply consists of the juxtaposition of these otherwise independent local pressure peaks.

4.2 Friction and clearance charts

In this section we explore parameter space for the selected configuration. Thousands of runs were made varying R between 4 and 1024, λ between 0.1 and 2, d between 0 and 10, and $S = 10^{-3}$ or $S = 0.5 \times 10^{-3}$.

4.2.1 R=32

Very little or no friction reduction appears for $R = 16$ or smaller. A bearing of $R = 32$ can be thus considered of moderate conformity for this configuration. Taking $m = m_0$ and $W^a = W_0^a$ the parameters are those of which one specific example was discussed as Case 1 of Section 4.1. For the specific depth $d = 5$ and the specific period $\lambda = 1$ we observed in Fig. 2 the pressure and saturation fields. The average friction coefficient $\bar{f}$ is 14% smaller for Case 1 than for an untextured runner. This significant improvement is however accompanied by an 7% loss in minimum clearance, suggesting an increase in wear.

It is interesting to see these values in the context of values obtained for all other possible textures, at least within some ranges. For this purpose, we performed 2500 simulations spanning the whole ranges of d and λ and plotted two-dimensional contours in the $d - \lambda$ plane in Fig. 5. The quantities plotted are:

- The relative variation V_f of the average friction coefficient, defined as

$$V_f(d, \lambda) = \frac{\bar{f}(d, \lambda) - f_{\text{untextured}}}{f_{\text{untextured}}}$$

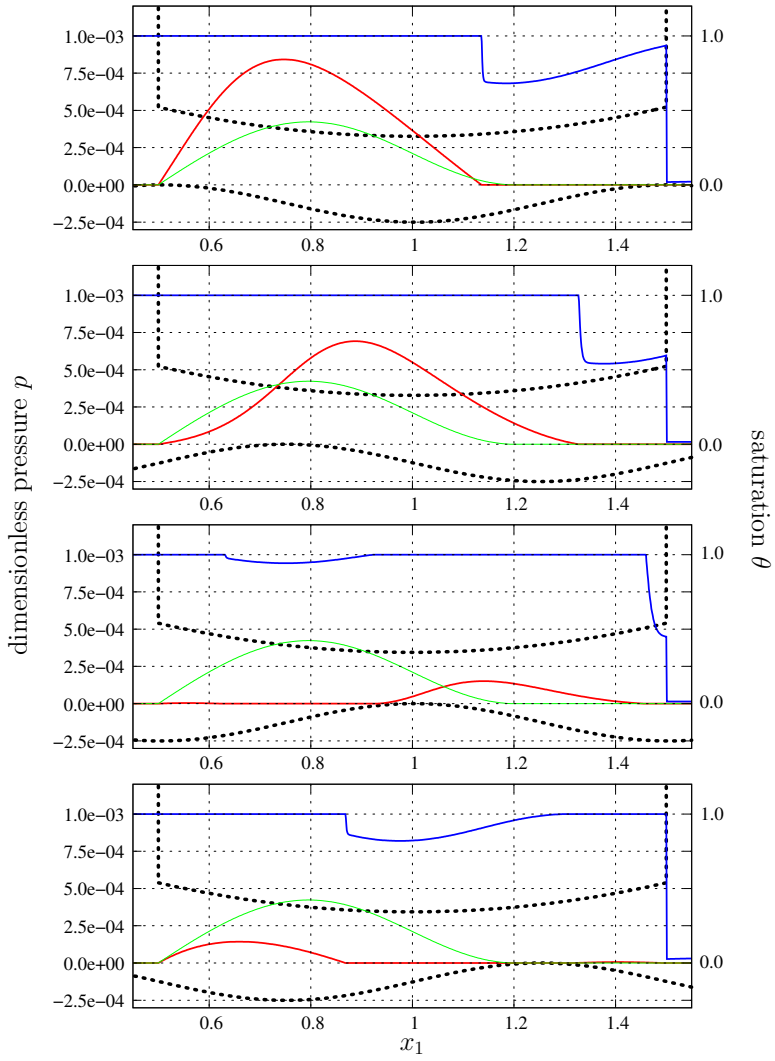

Figure 2: Instantaneous profiles of pressure p (in red) and saturation θ (in blue) for a bearing with $R = 32$, $d = 5$ and $\lambda = 1$ (Case 1 in the text) at $t = 0$, 0.25, 0.50 and 0.75 (from top to bottom) once the periodic regime has been attained. The steady pressure profile corresponding to the untextured runner is also plotted for comparison (in green).

- The relative variation V_C of the minimal clearance, defined as

$$V_C(d, \lambda) = \frac{C_{\min}(d, \lambda) - C_{\min,\text{untextured}}}{C_{\min,\text{untextured}}}$$

Please notice that the untextured case corresponds to the vertical axis of the plots ($d = 0$).

In Fig. 5(a) a contour map of V_f is shown. The axis $d = 0$ has obviously $V_f = 0$, and one observes that, depending on whether $\lambda > 0.5$ or not, V_f becomes negative or positive when the texture depth d is increased. For $\lambda > 0.5$ the friction diminishes as the texture is made deeper. Relative diminutions of about 30% can be seen at the top right corner of the chart, corresponding to $d = 10$ and $\lambda = 2$. Interestingly, for some given depth there exists an optimum period in terms of friction. It is roughly of value $\lambda = 1$ (texture's wavelength equal to the pad's length), but it increases with d to about 1.7 for

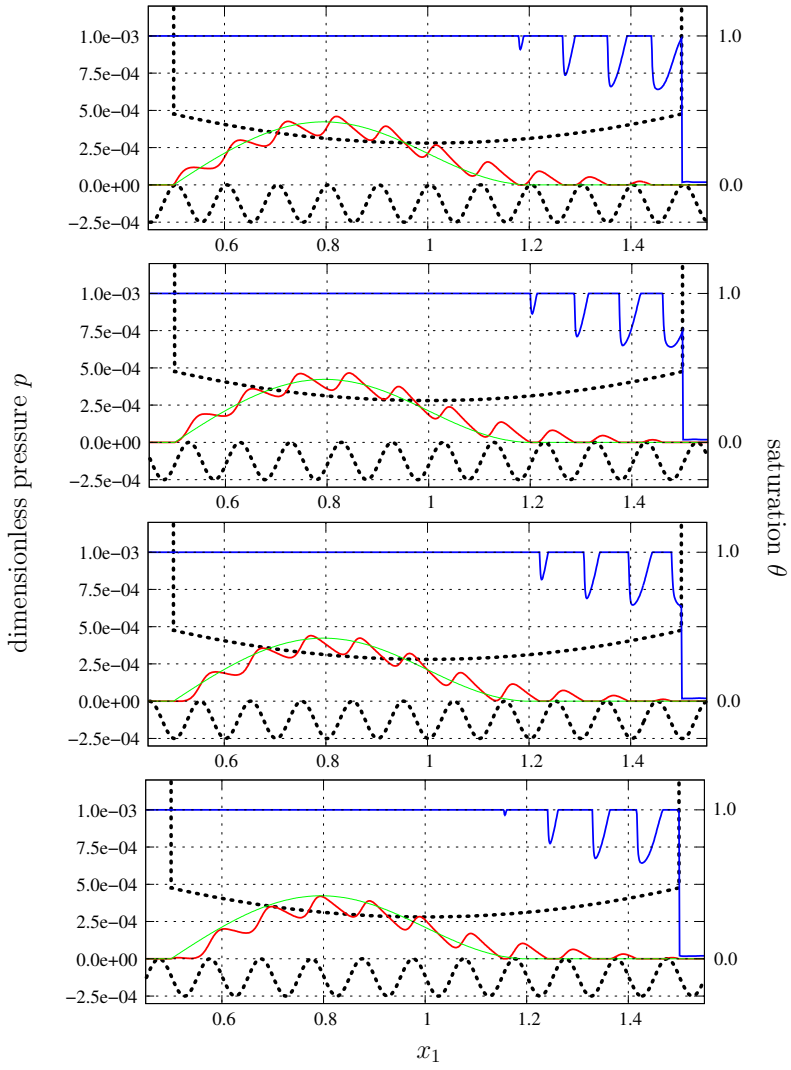

Figure 3: Instantaneous profiles of pressure p (in red) and saturation θ (in blue) for a bearing with $R = 32$, $d = 5$ and $\lambda = 0.1$ (Case 2 in the text) at $t = 0$, 0.025, 0.050 and 0.075 (from top to bottom) once the periodic regime has been attained. The steady pressure profile corresponding to the untextured runner is also plotted for comparison (in green).

$d = 10$. Notice that Case 1 discussed in Section 4.1 lies close to the optimum period for $d = 5$. From the position on the diagram one may conclude that Case 1 is indeed representative of the friction-reducing textures for pads with $R = 32$.

The contour map of V_C shown in Fig. 5(b), in turn, shows that all textures have minimal clearances smaller than that obtained with an untextured runner. Only negative values of V_C are observed in the chart.

An interesting phenomenon occurs at the bottom right sector of Figs. 5(a) and (b). Steep changes in $C_{\min}$ when d is varied around $d = 8$ are evident in the sector $\lambda < 0.2$. Significant variations of $\bar{f}$ are also observed there. The physics behind this phenomenon can be understood starting from Case 2 in Section 4.1, which has $d = 5$ and $\lambda = 0.1$. The texture-generated oscillations in the pressure field (see

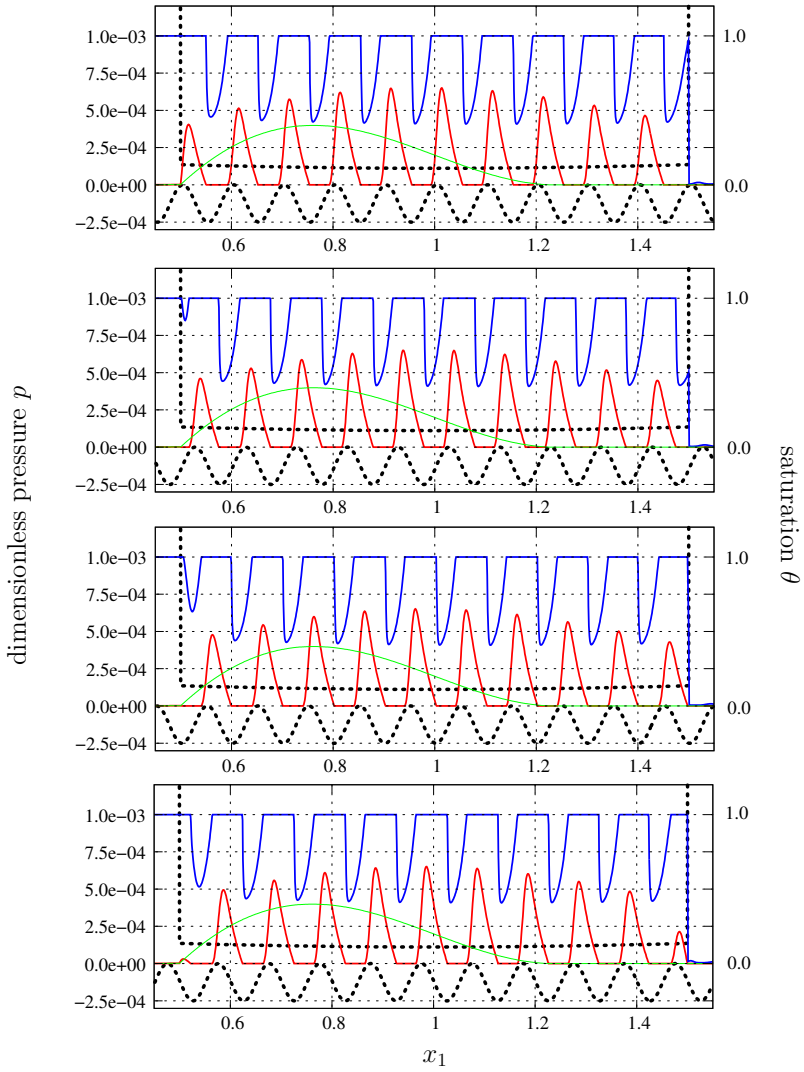

Figure 4: Instantaneous profiles of pressure p (in red) and saturation θ (in blue) for a bearing with $R = 256$, $d = 5$ and $\lambda = 0.1$ (Case 3 in the text) at $t = 0$, 0.025, 0.050 and 0.075 (from top to bottom) once the periodic regime has been attained. The pressure profile corresponding to the untextured runner is also plotted for comparison (in green).

Fig. 3) are superposed on the baseline pressurization curve generated by the pad's geometry, of which the pressure profile generated on the untextured runner provides an estimate. As d is increased keeping the other parameters fixed at the values of Case 2, some of the pressure oscillations touch the cavitation pressure and bubbles appear near the left edge of the pad. For $d = 8.15$ the p and θ profiles are as shown in Figure 6 (top graph). A bubble is seen to have grown on the left side of the pad. This cavitation bubble travels to the right with the divergent microwedge that generated it, but does not succeed to pass under the pad's center. Along its travel to the right, at some instant it gets pressurized and collapses (the value of θ goes back to 1 and the pressure becomes positive when the microwedge reaches $x \simeq 0.7$). One other bubble is generated at the same divergent wedge when it gets to $x \simeq 1.15$, as can be seen in the figure, which then travels until the right edge of the pad.

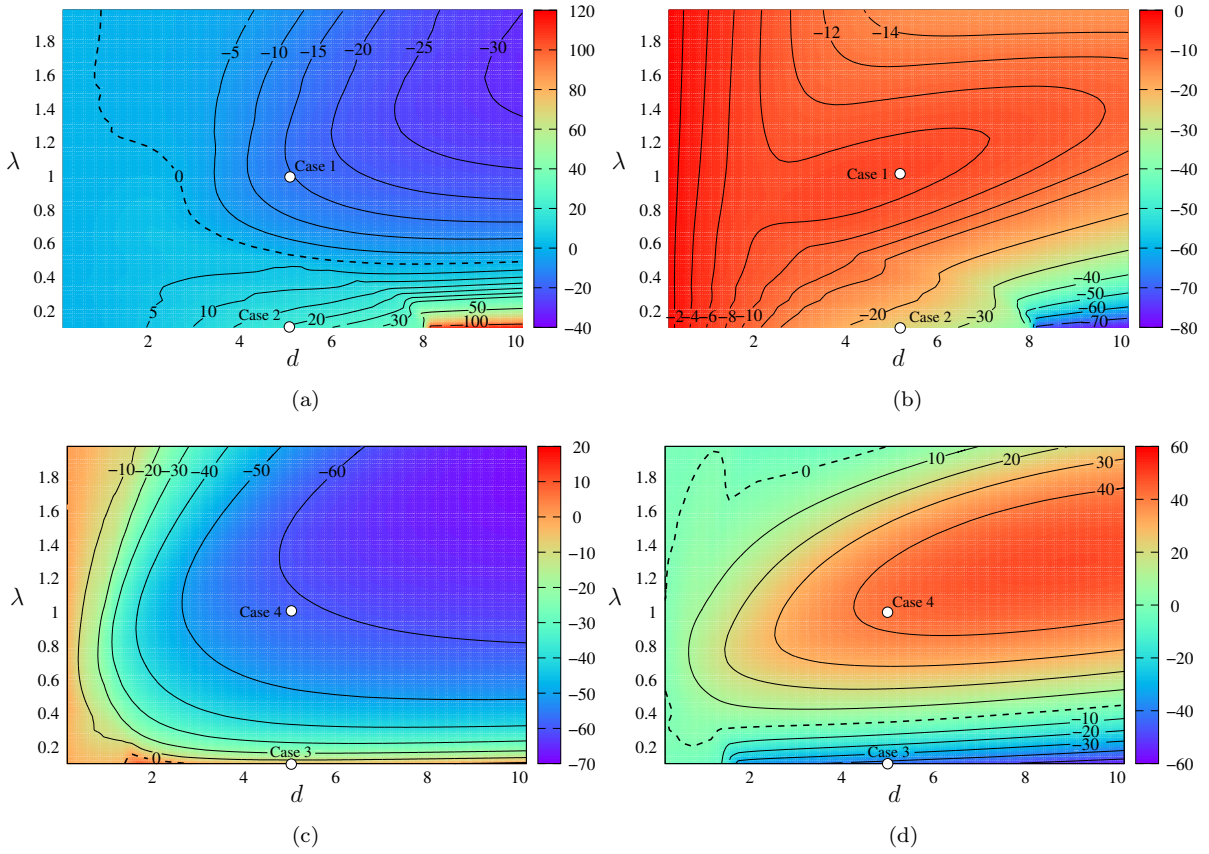

Figure 5: Relative differences (a) V_f and (b) V_C (expressed in percentages) with respect to the untextured runner, as functions of the texture parameters d and λ for a pad with R=32. The colorbars (as the isolines) indicate these percentages. Parts (c) and (d) of the Figure show analogous plots for R=256. All simulations computed with $W^a = W_0^a$ and $m = m_0$. The specific cases 1 to 4 discussed in the text are shown as white dots.

Between $d = 8.15$ and $d = 8.2$ a catastrophic event (in the mathematical sense) takes place. Increasing the texture depth makes the divergent microwedges steeper and the cavitation bubbles created near the inlet now travel under the pad without collapsing until the right edge. The pressure field undergoes a major change, since the relatively large pressurization region that existed between $x = 0.7$ and $x = 1.15$ now has disappeared. The pad looses lift and only re-encounters equilibrium at a much lower position. All these features can be seen in Fig. 6 (bottom graph). In Fig. 7 we plot the vertical movement of the pad as a function of time when the pad starts from the position $Z(0) = 4$. For $d \leq 8.15$ it climbs to values of Z of about 4.5, but for $d \geq 8.2$ it descends to about 2 units from the x-axis.

This interesting phenomenon, which does not depend on the model adopted for the friction force, suggests caution against carelessly increasing the depth of the texture, since tribological performance deteriorates substantially if this transition occurs. Experimental investigations could bring light onto the actual physical occurrence of this prediction of the Elrod-Adams model. Cases of high sensitivity of the friction coefficient to the texture depth have already been experimentally detected by Scaraggi *et al*[24].

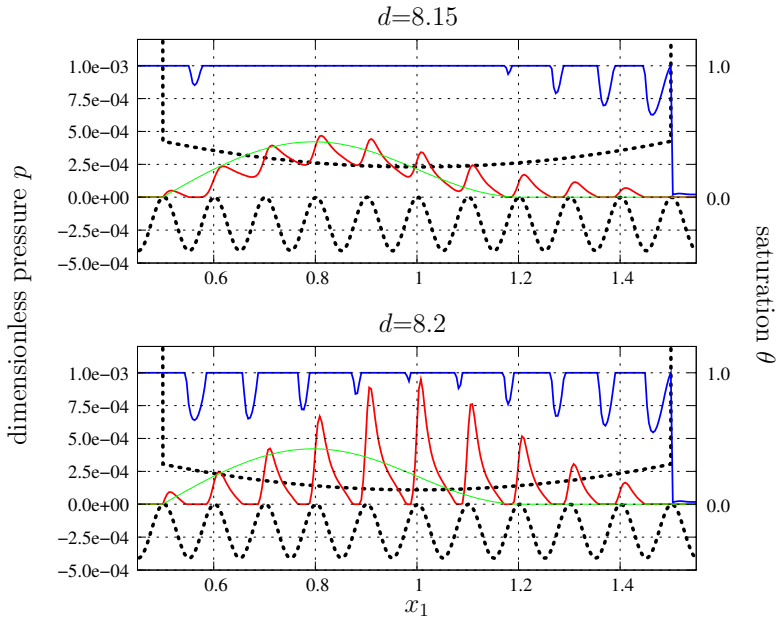

Figure 6: Profiles of p and θ in the periodic regime corresponding to bearings with λ=0.1, R=32, $m = m_0$ and $W^a = W_0^a$. The depth for the top graph is d=8.15 and for bottom one it is d=8.20.

4.2.2 R=256

Case 3 of Section 4.1 has $R = 256$, $d = 5$ and $\lambda = 0.1$. It corresponds to the central point of the horizontal axis in the graphs of V_f and V_C in Figs. 5 (c) and (d). Again, 2500 simulations were performed to compute the data for these graphs.

The value $R = 256$ corresponds to a high-conformity contact, in which the pressure field consists of a train of local pressurized regions (one at each convergent microwedge) traveling under the pad (see Fig. 4). Case 3 is an example of a poorly designed texture, because increasing the period λ a little (to 0.4 for example) would reduce the friction by about 40% while keeping the minimum clearance at a value similar to that of the untextured bearing. The best predicted performances in terms of both friction and wear correspond to $\lambda \simeq 1.5$ and $d = 10$.

In order not to depart too much from Cases 1-3 while investigating the friction-reducing sector of the charts, let us consider **Case 4**, which has the same runner as Case 1 but with the pad of Case 3; i.e.,

$$\textbf{Case 4:}\ R = 256, \qquad d = 5, \qquad \lambda = 1$$

For this bearing, the texture brings more than 60% improvement in friction together with 40% increase in minimum clearance, as compared to the untextured results. Instantaneous plots of pressure and saturation at $t = 0$, 0.25, 0.5 and 0.75 are shown in Fig. 8. Instead of the train of ten bubbles and ten pressure peaks translating under the pad as it was in Case 3, one now essentially observes a single cavitation bubble and a single pressurized region during most of the period. The larger size of the

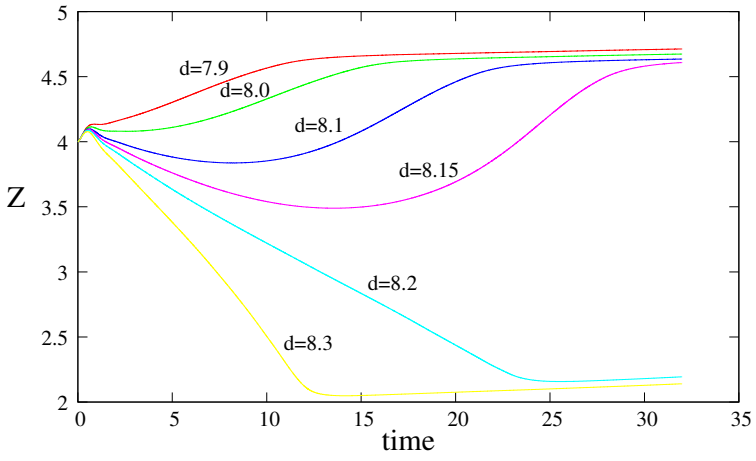

Figure 7: $Z(t)$ for textured bearings with λ=0.1, R=32, $m = m_0$ and $W^a = W_0^a$. Noticed the dramatic change in behavior when d changes from 8.15 to 8.20.

instantaneous pressurized region allows the pressure (and consequently the hydrodynamic force) to attain values comparable to those of the untextured case without diminishing (in fact, increasing) the clearance with respect to the untextured value. A comparison of $Z(t)$ and $F(t)$ for Cases 1 and 4 can be found in Fig. 9, where the complete evolution from an initial position $Z(0) = 4$ is shown (the instantaneous friction force is depicted just for one period). Notice that both cases, though having widely different values of R, have similar average F.

4.3 Increasing the load

A high sensitivity to the load is not a positive characteristic for a bearing. Even if the bearing works under constant *dimensional* load and at constant velocity, the *non-dimensional* load W^a is likely to vary in time because of its dependence on the viscosity of the lubricant.

To explore this issue, additional charts of V_f and V_C, analog to those of Fig. 5, were computed with twice the load, i.e., with $W^a = 2\,W_0^a$. The results can be found in Fig. 10. Let us compare part (a) of the figure, corresponding to V_f contours for $R = 32$, with its reference-load counterpart of Fig. 5(a). One sees that doubling the load makes the friction-reduction region in the $d - \lambda$ plane to shrink a little, but the global qualitative and quantitative trends are preserved. The abrupt transition discussed in the previous sections changes its location slightly, but otherwise the bearing performance is not severely affected by the change in load. Similar remarks can be made about the minimum clearance examining part (b) of Fig. 10.

The weak sensitivity of $V_f(d, \lambda)$ to W^a is also evident from the chart corresponding to $R = 256$, which is found in Fig. 10(c). The chart of V_C, in turn (Fig. 10(d)), in turn, exhibits some more sensitivity to the load. The maximum relative gain in V_C, which is more than 40% for the reference load, reduces to about 25% for $W^a = 2\,W_0^a$. The beneficial effect of the texture of Cases 1 and 4 is nevertheless

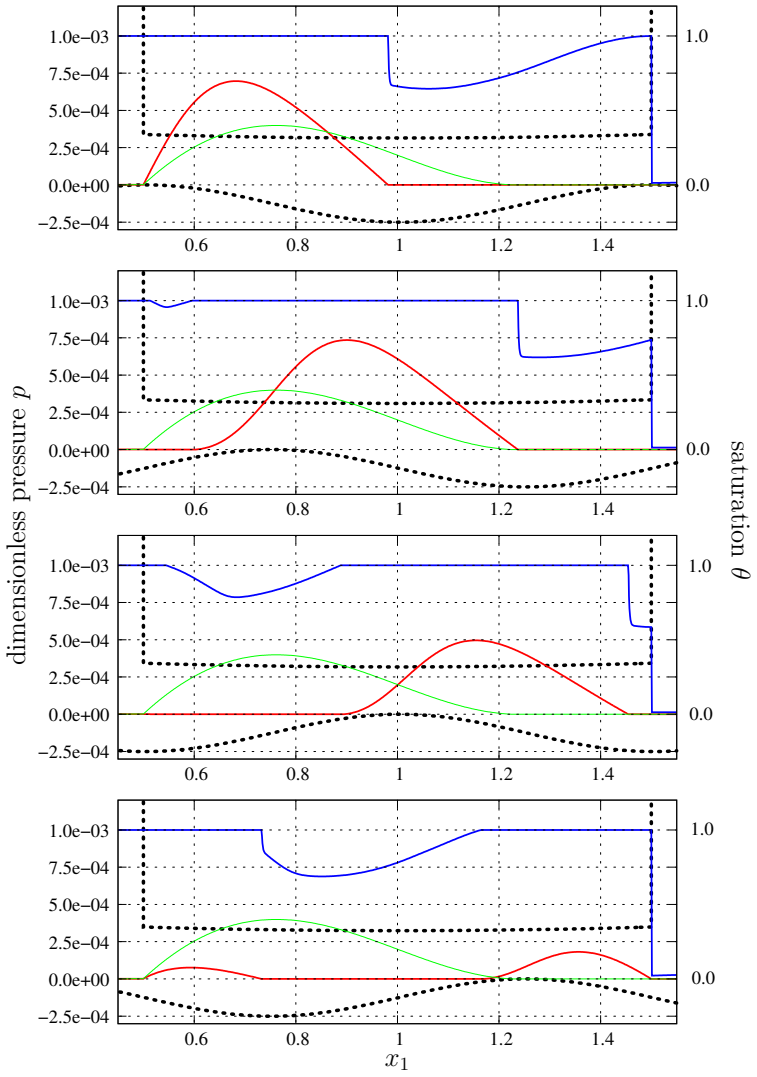

Figure 8: Instantaneous profiles of pressure p (in red) and saturation θ (in blue) for a bearing with $R = 256$, $d = 5$ and $\lambda = 1$ (Case 4 in the text) at $t = 0$, 0.025, 0.050 and 0.075 (from top to bottom) once the periodic regime has been attained. The pressure profile corresponding to the untextured runner is also plotted for comparison (in green).

maintained at this larger load.

5 DISCUSSION OF RESULTS

For low-conformity bearings ($R/L \leq 16$) the results above confirm that no beneficial effects in either friction or wear are predicted by the model, which is consistent with previous findings [2–4].

For moderate- ($R/L = 32$) and high-conformity ($R/L = 256$) bearings, on the other hand, the two-dimensional contour plots of friction and clearance together with the specific simulations (cases 1-4) selected for detailed scrutiny, revealed some *general* trends and underlying physical mechanisms:

1. Friction coefficients of high-conformity bearings are greater than those of moderate-conformity

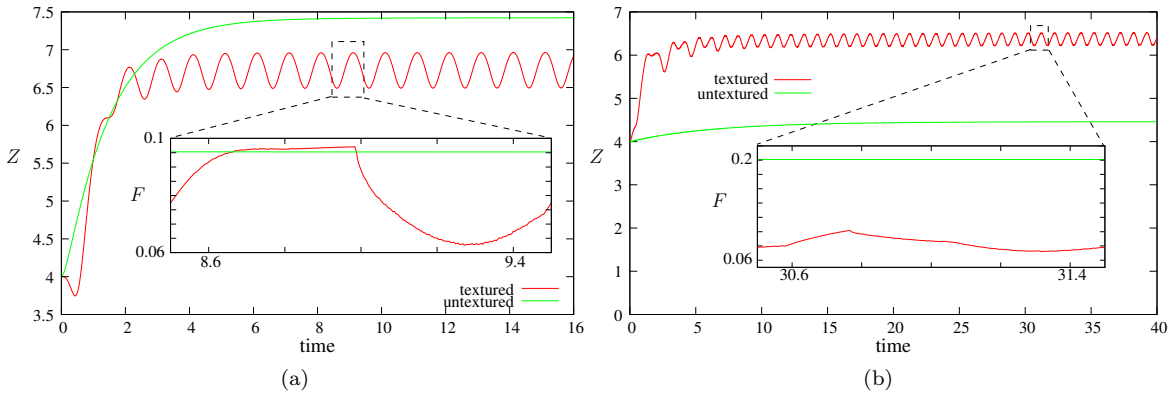

Figure 9: Ring position $Z(t)$ and friction force $F(t)$ (detail in figure) for rings with a curvature radius R of (a) 32 (b) 256. The texture parameters are λ=1.0 and d=5. Notice that (a) corresponds to Case 1 in the text, while (b) corresponds to Case 4.

ones. In both cases, textures of period comparable to the pad's length and sufficiently deep seem to be optimal in terms of friction for the ranges considered. The mathematical model predicts a relative reduction of friction of up to 40% for moderate-conformity bearings and up to 75% for high-conformity ones.

2. The optimal period (in terms of friction and wear) for each depth d is predicted to be comparable to the pad's length ($\lambda \simeq 1$) and a slowly increasing function of d.

3. Though textures can indeed reduce the friction of moderate-conformity bearings, all textured runners produce pad-to-runner clearances that are smaller than that of the untextured runner.

4. Suitable textures significantly improve the clearance of high-conformity bearings (by 20% or more), thus predicting reductions in wear.

5. The basic mechanism of friction reduction is a local pressurization of the convergent microwedges at each texture cell, accompanied by local cavitation at the divergent microwedges. The cavitation bubble that forms at each texture cell prevents the appearance of local negative pressure peaks that would cancel out the positive lift force generated at the convergent microwedges. The extra lift generated in this way increases the clearance and reduces friction.

6. This explains why longer texture periods (wavelengths of order L) are predicted to be more efficient than shorter ones, since the capacity of a wedge to generate lift increases with length.

7. Best performance is achieved when the depth is of the order of twice the pad's fly height Z, so that the convergent microwedge (which has film thickness $Z + d$ at the trough and Z at the crest, approximately) has taper ratio $(Z + d)/Z$ in the range $2.5 - 3.5$. Taper ratios in this range are known to be effective not only for generating load capacity (the Rayleigh step, which is optimal, has a slightly smaller taper ratio of 1.866) but also for minimizing friction [25].

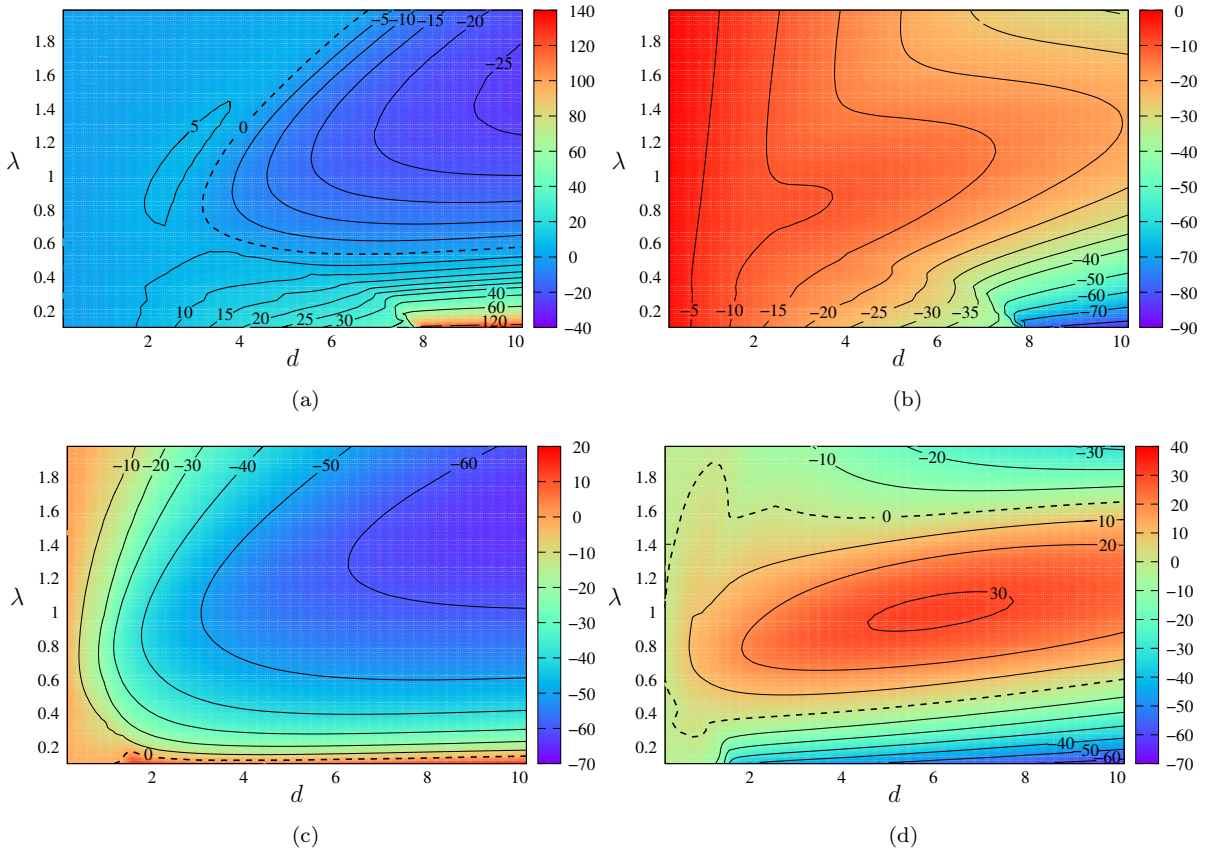

Figure 10: Same organization of results as in Fig. 5, but changing the applied load to $W^a = 2\,W_0^a$.

8. To prove the previous assertion, let us present the results in Figs. 5 and 10 in another way. For each period λ there is a depth $d_f(\lambda)$ that minimizes friction, which is shown in Fig. 11. For $R = 256$, the minimal-friction depth $d_f(\lambda)$ is zero, corresponding to the untextured runner, only for periods smaller than 0.15. For $\lambda > 0.15$ one observes $d_f(\lambda)$ increasing steadily with λ. A similar trend is observed for $R = 32$, though in this case the untextured runner is optimal until λ is about 0.5 (depending on the charge). There is also a corresponding minimal clearance, $C_{\min}(d_f(\lambda), \lambda)$, with can be taken as a representative value for the pad's fly height. One can thus plot the taper ratios corresponding to minimal friction for each λ, which is given by

$$t_f(\lambda) = \frac{C_{\min}(d_f(\lambda), \lambda) + d_f(\lambda)}{C_{\min}(d_f(\lambda), \lambda)} \tag{21}$$

This is done in Fig. 12 for $R = 32$ and $R = 256$ and for loads $W^a = W_0^a$, $W^a = 2\,W_0^a$ and $W^a = 3\,W_0^a$. Consider first the curve corresponding to $R = 256$ and $W^a = W_0^a$. The taper ratio that yields minimal friction is remarkably constant from $\lambda = 0.2$ up to $\lambda = 1.4$, taking values in the range 2.5–3.5. As the load is increased, and although $d_f(\lambda)$ decreases accordingly (see Fig. 11), the optimal taper ratio remains in the same range (2.5–3.5) but up to a smaller value of λ (up to $\lambda = 1.2$ for $W^a = 2\,W_0^a$ and up to $\lambda = 1$ for $W^a = 3\,W_0^a$). One thus concludes that for

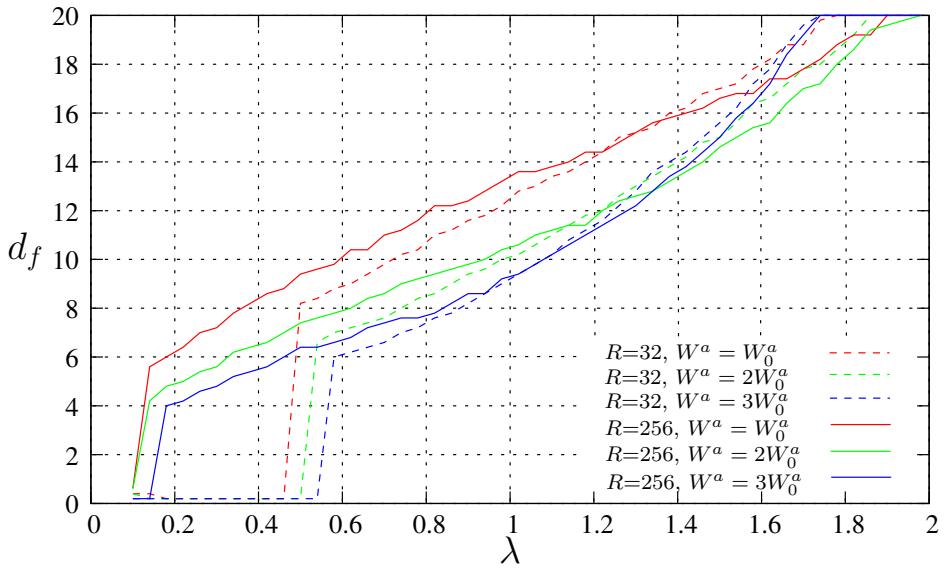

Figure 11: Texture depth corresponding to minimal friction $d_f(\lambda)$ as a function of the period λ. Shown are numerical data corresponding to $R = 32$ and $R = 256$, in each case considering loads $W^a = W_0^a$, $W^a = 2\,W_0^a$ and $W^a = 3\,W_0^a$.

highly-conformal bearings the Elrod-Adams model suggests selecting the texture depth so that the taper ratio is between 2.5–3.5, which corresponds to d in the range between $1.5\,C_{\min}$ and $2.5\,C_{\min}$.

9. For the case $R = 32$ one observes that the untextured runner is optimal up to $\lambda \simeq 0.5$ (in fact, 0.45 for $W^a = W_0^a$ and 0.55 for $W^a = 3\,W_0^a$). At $\lambda \simeq 0.5$ the optimal taper ratio $t_f(\lambda)$ undergoes a jump to a value of about 2.5 and from there increases steadily with λ, remaining below 3.5 up to $\lambda = 1$. The model thus again suggests to take d in the range $1.5\,C_{\min} - 2.5\,C_{\min}$, though only for texture periods larger than half the pad's length this time.

10. Since $d/C_{\min}$ must be $\simeq 1.5 - 2.5$ to be effective, larger loads require shallower textures. This puts forward the challenge in designing textures for variable loads.

11. An interesting behavior is predicted for textures with short wavelength ($\lambda < 0.25$). As the depth d is increased, cavitation bubbles begin to form at the left edge of the pad over each divergent microwedge. Each of these bubbles travels with the wedge that generated it, but it collapses under the pressurization effect of the converging part of the pad. When the wedge gets to the divergent part of the pad, a new bubble forms on it and travels with it until reaching the right edge of the pad. This leaves a central portion of the pad pressurized.

12. For moderate-conformity bearings, the previous behavior persists until the depth reaches a limit value of about $d = 8$. If d is further increased, the bubbles no longer collapse under the pad and the central pressurized portion of the pad no longer exists. As a consequence, the clearance is severely reduced (by up to 50%!). This sudden transition should be further investigated by experimental

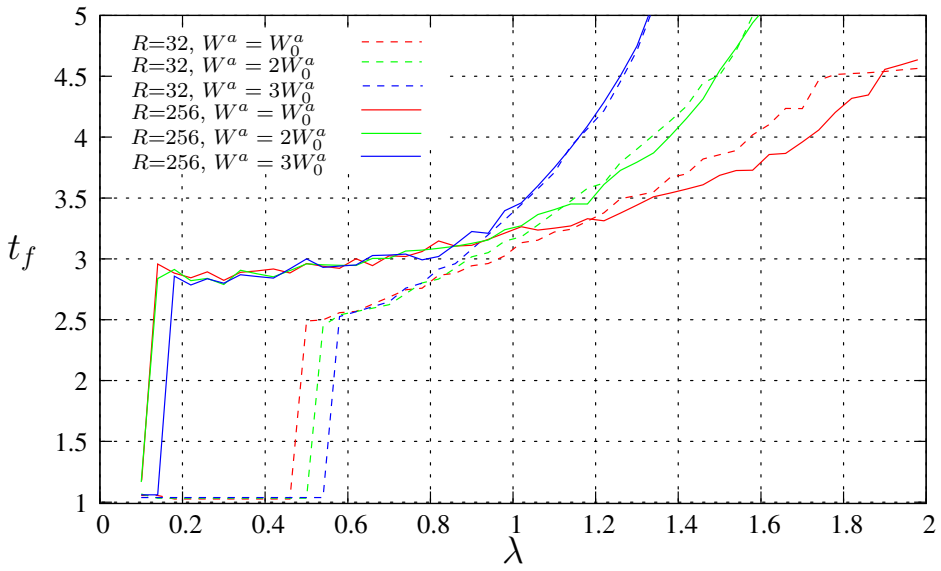

Figure 12: Taper ratio corresponding to minimal friction $t_f(\lambda)$ as a function of the period λ. Shown are numerical data corresponding to $R = 32$ and $R = 256$, in each case considering loads $W^a = W_0^a$, $W^a = 2\,W_0^a$ and $W^a = 3\,W_0^a$.

techniques, since our results are model dependent.

13. For high-conformity bearings a similar transition occurs, but at a much lower value of d.

6 Conclusions

An extensive study has been reported on the effect of transverse sinusoidal textures on the tribological performance of an infinitely-wide thrust bearing with the texture on the runner. Contacts with different conformity were considered by varying the ratio R/L, with R the curvature radius of the pad and L its length. The analysis method consists of time- and mesh-resolved simulations (with up to 4096 cells in the longitudinal direction and 40000 time steps) with a finite volume approximation of the Elrod-Adams model.

Upon non-dimensionalization, the problem depends on the mass of the pad m and the load applied on it, W^a. For these variables values representative of piston ring/liner contacts were assumed. The remaining two free parameters are those defining the texture: its depth d and its period λ. More than ten thousand simulations were run to construct two-parameter frictional and clearance charts for the ranges $0 \leq d \leq 10$ and $0.1 \leq \lambda \leq 2$, and some selected cases were subject to detailed scrutiny.

The analysis of these simulations confirmed that textures are predicted to be beneficial only for contacts with moderate or high conformity ($R/L \geq 32$). The mechanism involved in friction reduction was identified as the local pressurization of the convergent wedge present in each texture cell, in agreement with the mechanism proposed earlier for *stationary* textures[1,26] (corresponding to a textured pad in our

setting). The bearing's response to the texture, at least as predicted by Elrod-Adams model, indicates that best performance is obtained with texture lengths comparable to the pad's length, and with depths of approximately twice the pad-to-runner clearance. Though these conclusions were drawn considering just one value of the pad's mass ($m = m_0$), it was confirmed that they remain valid for twice and half this value ($m = 2m_0$ and $m = m_0/2$), though this complementary study was not included here for the sake of brevity. Other general observations were collected and discussed in Section 5.

Further numerical investigations extending the ranges of the study reported here can of course unveil new phenomena, which of course would depend on the physical validity of the adopted model. In fact, our numerical assessment suggests as possible validation the investigation of a sudden transition in clearance that is predicted as the texture depth is increased under specific operating conditions.

7 Acknowledgments

This work was supported by Coordenação de Aperfeiçoamento de Pessoal de Nível Superior [grant number DS-8434433/M] (Brazil), by Fundação de Amparo à Pesquisa do Estado de São Paulo [grants numbers 2012/14481-8, 2011/24147-5] (Brazil), by Conselho Nacional de Desenvolvimento Científico e Tecnológico [grant number 308728/2013-0] (Brazil) and by Renault (France).

References

1 Dobrica MB, Fillon M, Pascovici MD, Cicone T. Optimizing surface texture for hydrodynamic lubricated contacs using a mass-conserving numerical approach. Proc IMechE. 2010;224:737–750.

2 Gadeschi GB, Backhaus K, Knoll G. Numerical analysis of laser-textured piston-rings in the hydrodynamic lubrication regime. ASME Journal of Tribology. 2012; 134:041702–1–041702–8.

3 Etsion I. Modeling of surface texturing in hydrodynamic lubrication. Friction. 2013; 3:195–209.

4 Checo H, Ausas R, Jai M, Cadalen JP, Choukroun F, Buscaglia G. Moving textures: Simulation of a ring sliding on a textured liner. Tribology International. 2014; 72:131–142.

5 Buscaglia GC, Ciuperca I, Jai M. The effect of periodic textures on the static characteristics of thrust bearings. ASME Journal of Tribology. 2005; 127:899–902.

6 Buscaglia G, Ciuperca I, Jai M. On the optimization of surface textures for lubricated contacts. Journal of Mathematical Analysis and Applications. 2007; 335:1309–1327.

7 Costa HL, Hutchings IM. Hydrodynamic lubrication of textured steel surfaces under reciprocating sliding conditions. Tribology International. 2007; 40:1227–1238.

8 Kovalchenko A, Ajayi O, Erdemir A, Fenske G. Friction and wear behavior of laser textured surface under lubricated initial point contact. Wear. 2011; 271:1719–1725.

9 Bifeng Y, Li X, Fu Y, Yun W. Effect of laser textured dimples on the lubrication performance of cylinder liner in diesel engine. Lubrication Science. 2012; 24:293–312.

10 Tomanik E. Modelling the hydrodynamic support of cylinder bore and piston rings with laser textured surfaces. Tribology International. 2013; 59:90–96.

11 Scaraggi M, Mezzapesa FP, Carbone G, Ancona A, Tricarico L. Friction properties of lubricated laser-microtextured-surfaces: an experimental study from boundary to hydrodynamic lubrication. Tribology Letters. 2013; 49:117–125.

12 Qiu Y, Khonsari M. Experimental investigation of tribological performance of laser textured stainless steel rings. Tribology International. 2011; 44:635–644.

13 Grabon W, Koszela W, Pawlus P, Ochwat S. Improving tribological behavior of piston ring-cylinder liner frictional pair by liner surface texturing. Tribology International. 2013; 61:102–108.

14 Cross AT, Sadeghi F, Rateick RG, Rowan S. Hydrodynamic pressure generation in a pocketed thrust bearing. Tribology Transactions. 2013; 56:652–662.

15 Zhang J, Meng Y. Direct observation of cavitation phenomenon and hydrodynamic lubrication analysis of textured surfaces. Tribology Letters. 2012; 46:147–158.

16 Ausas RF, Jai M, Ciuperca IS, Buscaglia GC. Conservative one-dimensional finite volume discretization of a new cavitation model for piston-ring lubrication. Tribology International. 2013; 57:54–66.

17 Buscaglia GC, Ciuperca I, Dalissier E, Mohammed J. A new cavitation model in lubrication:the case of two-zone cavitation. Journal of Engineering Mathematics. 2013; 83:57–79.

18 Ausas R, Ragot P, Leiva J, Jai G M Bayada, Buscaglia G. The impact of the Cavitation model in the Analysis of Micro-Textured Lubricated Journal bearings. ASME Journal of Tribology. 2009; 129:868–875.

19 Ausas R, Jai M, Buscaglia G. A Mass-Conserving Algorithm for Dynamical Lubrication Problems With Cavitation. ASME Journal of Tribology. 2009; 131:031702-1–031702-7.

20 Fowell M, Olver A, Gosman A, Spikes H, Pegg I. Entrainment and Inlet Suction: Two Mechanisms of Hydrodynamic Lubrication in Textured Bearings. ASME Journal of Tribology. 2007; 129:336–347.

21 Elrod HG, Adams M. A computer program for cavitation. Technical report 190. 1st LEEDS LYON Symposium on Cavitation and Related Phenomena in Lubrication, IME. 1974; 103:354.

22 Fulton SR, Ciesielsky PE, Schubert WH. Multigrid methods for elliptic problems: a review. Monthly Weather Review. 1986; 114:943–959.

23 Venner CH, Lubrecht AA. Multilevel methods in lubrication. Elsevier; 2000.

24 Scaraggi M, Mezzapesa F, Carbone G, Ancona A, Sorgente D, Lugar P. Minimize friction of lubricated laser-microtextured-surfaces by tuning microholes depth. Tribology International. 2014; 75:123–127.

25 Rahmani R, Shirvani A, Shirvani H. Analytical analysis and optimization of the Rayleigh step slider bearing. Tribology International. 2009; 42:666–674.

26 Etsion I. State of the art in laser surface texturing. ASME Journal of Tribology. 2005;127:248–253.

List of Figures